The moiré potential in twisted transition metal dichalcogenide bilayers

Christopher Linderälv,[1] Joakim Hagel,[1] Samuel Brem,[2] Ermin Malic,[2,1] and Paul Erhart[1,*]

[1] *Department of Physics, Chalmers University of Technology, SE-41296, Gothenburg, Sweden*
[2] *Department of Physics, Philipps University of Marburg, 35037 Marburg, Germany*

Moiré superlattices serve as a playground for emerging phenomena, such as localization of band states, superconductivity, and localization of excitons. These superlattices are large and are often modeled in the zero angle limit, which obscures the effect of finite twist angles. Here, by means of first-principles calculations we quantify the twist-angle dependence of the moiré potential in the MoS_2 homobilayer and identify the contributions from the constituent elements of the moiré potential. Furthermore, by considering the zero-angle limit configurations, we show that the moiré potential is rather homogeneous across the transition metal dichalcogenides (TMDs) and briefly discuss the separate effects of potential shifts and hybridization on the bilayer hybrid excitons. We find that the moiré potential in TMDs exhibits both an electrostatic component and a hybridization component, which are intertwined and have different relative strengths in different parts of the Brillouin zone. The electrostatic component of the moiré potential is a varying dipole field, which has a strong twist angle dependence. In some cases, the hybridization component can be interpreted as a tunneling rate but the interpretation is not generally applicable over the full Brillouin zone.

I. INTRODUCTION

Hexagonal bilayer transition metal dichalcogenides (TMDs) with a rotational misorientation between the monolayer sheets can exhibit an interference pattern in the atomic positions known as a moiré pattern. The latter can alter the electronic structure of the twisted TMD bilayer and lead to, e.g., localized electronic[1] and excitonic states.[2] Since the moiré unit cell at low twist angles (for a lattice constant matched bilayer) becomes very large, such structures are very demanding to simulate with first-principles calculations.

Density functional theory (DFT)-based first-principles calculations of the *ground state* of moiré structures have revealed localized electronic states.[1] It is, however, computationally much more difficult to access electronic *excitations* within such a framework. Hence, tight-binding models[3] remain the most feasible route to access electronic properties of twisted bilayers at low angles.

The twisting induces a moiré pattern with spatially varying local stacking orders (Fig. 1a). There are three locations within the moiré unit cell where the local environment exhibits high symmetry (threefold rotational symmetry), which can be modeled by stacking the atoms accordingly in the primitive bilayer cell (Fig. 1a). This method for analyzing twist-induced phenomena in TMDs has been used in, e.g., Refs. 2–5. The caveat of this method is that it is strictly valid only at very low twist angles since for shorter moiré periods the atomic arrangement changes rapidly away from the high symmetry points. Therefore, it is of importance to quantify the twist angle dependence of the induced potential.

Furthermore, in order to construct more accurate tight-binding models the electrostatic part of the moiré potential needs to be disentangled from the tunneling contribution, which calls for a deeper investigation of the electronic structure of the limiting configurations. This includes a more careful study of the actual origin and nature of the moiré potential, and recently several studies emerged targeting the fundamental properties of the moiré potential. Specifically, the moiré potential in $MoSe_2/WSe_2$ heterobilayers has been shown to be on the order of 150 to 300 meV and dominated by planar strain,[6] and the band gap in $MoS_2/MoTe_2$ has been observed to be strongly twist-angle dependent.[7] A comprehensive description that connects the aforedescribed observations and establishes general trends that hold across different combinations of TMDs is, however, still needed.

Here, we therefore assess the moiré potential via first-principles calculations both on explicit moiré configurations and limiting configurations based on the primitive unit cell (Fig. 1). We aim to provide a unifying perspective of the moiré potential in TMDs, in particular of the origin of the potential and the similarity of the potential in different bilayer systems. Finally, we disentangle the electrostatic part of the moiré potential and determine the hybridization contribution at high symmetry points in the moiré superlattice.

II. METHODOLOGY

In order to construct the explicit moiré superlattices we have used the method outlined in Ref. 8. The commensurate hexagonal moiré superlattices are found at angles[8]

$$\theta_k = \arccos\left(\frac{3k^2+3k+0.5}{3k^2+3k+1}\right), \tag{1}$$

where k is a non-negative integer. In this work, we consider values up to $k = 7$, corresponding to an angle of 4.41°. The variations in the local atomic environment give rise to an electrostatic potential that varies in the plane of the monolayer sheets, which we denote as the *intralayer* moiré potential. By definition, the difference of the *intralayer* moiré potentials in the two adjacent layers is the *interlayer* moiré potential.[7]

We consider two different measures of the electrostatic potential induced by twisting: (1) The (average) elec-

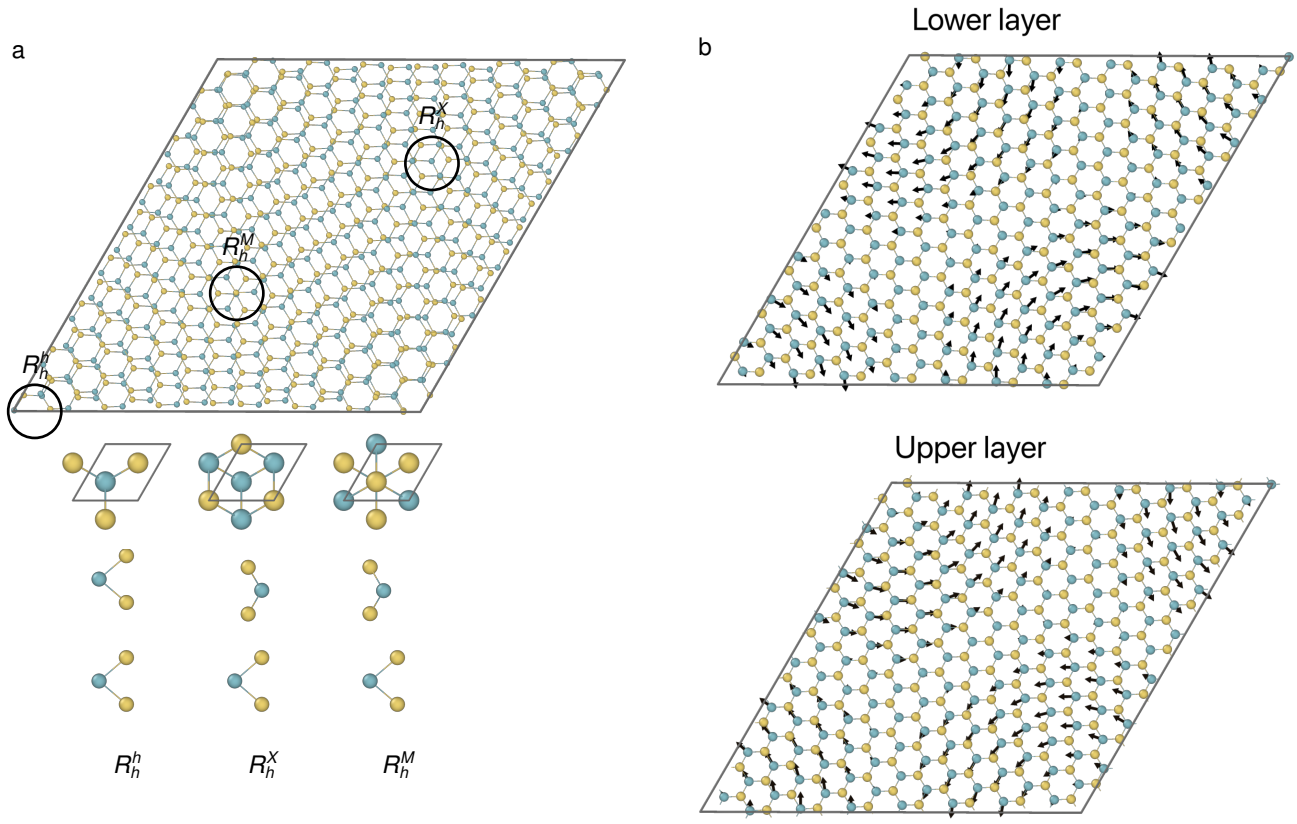

FIG. 1. (a) The explicit MoS_2 homobilayer moiré structure at a twist angle of $\theta = 2.9^\circ$ along with the limiting ($\theta \to 0^\circ$) local registry at three specific points. Blue (yellow) atoms indicate atomic species Mo (S). (b) Lateral relaxation for the MoS_2/MoS_2 homobilayer twisted 4.41°. The arrows are amplified with a factor of 30.

trostatic core potential is a measure of the local electrostatic environment of the relevant electronic states, which in TMDs are primarily composed of d orbitals of the transition metal.[9] (2) The second measure, which is closely related to the first is the induced dipole field.[10] It is strictly applicable only to the limiting configurations, since in explicit moiré superlattices, the field exhibits higher moments. The charge density difference upon bilayer formation is

$$\delta n(\boldsymbol{r}) = n(\boldsymbol{r}) - \sum_i n_i(\boldsymbol{r}), \tag{2}$$

where $n(\boldsymbol{r})$ is the charge density of the bilayer structure and $n_i(\boldsymbol{r})$ denotes the charge densities of the constituent monolayers. The charge density difference δn gives rise to a potential δV. In order to accurately determine the potential δV and the induced vacuum level difference D

$$D = \delta V(-\infty) - \delta V(\infty), \tag{3}$$

dipole corrections are added when solving the Poisson equation for the electron density.

In order to estimate how δV affects different single particle states we compute the following matrix elements for the monolayer states In order to estimate how δV affects different single particle states we compute the following matrix elements for the monolayer states

$$M^L_{n\boldsymbol{k}} = \langle \psi^L_{n\boldsymbol{k}} | \delta V | \psi^L_{n\boldsymbol{k}} \rangle, \tag{4}$$

where L is the monolayer index and n is either v (valence band) or c (conduction band). In the spirit of perturbation theory, $M^L_{n\boldsymbol{k}}$ is the first-order shift of the state $n\boldsymbol{k}$ in monolayer L due to the induced electrostatic potential. The (average) hybridization contribution to the level shift upon bilayer formation is then computed as

$$\Delta_{n\boldsymbol{k}} = \frac{1}{2}\Big[\varepsilon^{\text{bilayer},+}_{n\boldsymbol{k}} - \varepsilon^{\text{bilayer},-}_{n\boldsymbol{k}} - \left(M^+_{n\boldsymbol{k}} - M^-_{n\boldsymbol{k}} + \Delta\varepsilon^{\text{mono}}_{n\boldsymbol{k}}\right)\Big], \tag{5}$$

where $\varepsilon^{\text{bilayer},+}_{n\boldsymbol{k}}$ is the energy of the bilayer state that shifts towards larger energies, $M^+_{n\boldsymbol{k}}$ is the matrix element in the layer which experiences a positive potential, and $\Delta\varepsilon^{\text{mono}}_{n\boldsymbol{k}}$ is the energy level difference between the monolayers (which is zero for homobilayers). We will also make

use of the (average) interlayer tunneling rate

$$T^2_{n\boldsymbol{k}} = \frac{1}{2}\Big[\left(\varepsilon^{\text{bilayer},+}_{n\boldsymbol{k}} - \varepsilon^{\text{bilayer},-}_{n\boldsymbol{k}}\right)^2 - \left(M^+_{n\boldsymbol{k}} - M^-_{n\boldsymbol{k}} + \Delta\varepsilon^{\text{mono}}_{n\boldsymbol{k}}\right)^2\Big], \quad (6)$$

which may be interpreted as the off-diagonal perturbation of a two-level system. These tunneling strengths may be, e.g., included in a tight-binding model for the exciton energies of twisted structures.[2]

For the purpose of this paper, we consider a simpler case of untwisted structures to disentangle the effect of electrostatic effects and hybridization.[11] To this end, we use the exciton density matrix formalism[12–14] and calculate the exciton energies for untwisted van-der-Waals heterostructures by first formulating a Hamiltonian in second quantization for the interaction free electronic energies

$$H = \sum_{\alpha l\boldsymbol{k}} \tilde{E}^{\alpha s}_{l\boldsymbol{k}} a^\dagger_{\alpha l\boldsymbol{k}} a_{\alpha l\boldsymbol{k}} + \sum_{\alpha \boldsymbol{k} l\neq l'} T^{\alpha s}_{ll'} a^\dagger_{\alpha l\boldsymbol{k}} a_{\alpha l\boldsymbol{k}}, \quad (7)$$

where l, l' are layer indices, $\alpha = (\lambda, \xi)$ is a compound index with ξ denoting the valley and $\lambda = (c, v)$ the conduction and the valence band respectively. Here $a^\dagger$ (a) denotes the electronic creation (annihilation) operator. The possible excitonic transitions in this way are illustrated in Fig. 2. Here, $\boldsymbol{k}$ is the electronic wave vector and s is the stacking index. $\tilde{E}^{\alpha s}_{l\boldsymbol{k}}$ are the electronic energies as well as the electrostatically induced alignment shifts. $T^{\alpha s}_{ll'}$ is the tunneling matrix element, which is modeled following a tight-binding approach.[15,16] Consequently, the tunneling matrix element are directly proportional to the tunneling strength for those stackings, for which tunneling is allowed by C_3 symmetry. By following the method laid out in Refs. 15 and 2, the Hamiltonian is transformed into an exciton basis, thus taking into account the binding energies. The final hybrid exciton energies are calculated by first transforming into a hybrid basis $Y^\dagger_{\xi\eta} = \sum_L \mathcal{C}^{\xi\eta}_L(Q)^* X^\dagger_{\xi LQ}$, which consists of a linear combination of the intra and interlayer exciton contributions $\mathcal{C}^{\xi\eta}_L(Q)$ to the final hybrid state. Here, L is a compound layer index, Q is the center-of-mass momentum, η the new band index and $X^\dagger$(X) are the exciton creation(annihilation) operators. The eigenvalue problem that arises in order to diagonalize this new hybrid exciton Hamiltonian yields the final exciton energies.

DFT calculations were performed using the projector augmented wave method[17] while atomic configurations were prepared and analyzed using ASE.[18] All structural relaxations were carried out using VASP[19,20] and the vdW-DF-cx method.[21,22] The monolayer lattice parameters were obtained using a plane wave cutoff of 340 eV and a $\boldsymbol{k}$-point mesh with a density of 0.3 Å^{-1}. The atomic positions for the limiting bilayer structures (Fig. 1) were relaxed using the same functional but with a cutoff energy of 500 eV and a $18 \times 18 \times 1$ $\boldsymbol{k}$-point mesh until the maximum force acting on any atom was less than 2.5 meV Å^{-1}. The explicit moiré superlattices with up to 1,014 atoms were relaxed using a plane wave cutoff of 340 eV until the maximal force acting on any ion was less than 7.5 meV Å^{-1}. The cell vector in the out-of-plane direction was 70 Å for these configurations to ensure decoupling across periodic boundary conditions.

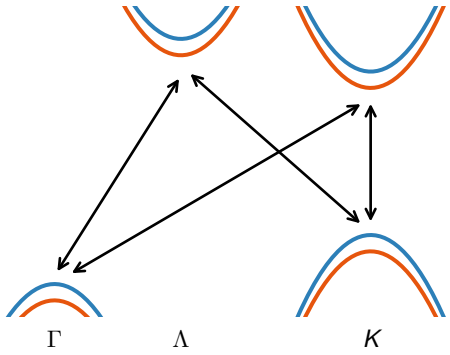

FIG. 2. Schematic illustration of the possible excitonic transitions considered here with a band arrangement that corresponds to the case of non-interacting monolayers with type II band alignment. The $K-K$ exciton is a direct exciton, whereas the other considered excitons ($K-\Lambda$, $\Gamma-\Lambda$, $\Gamma-K$) are indirect in momentum.

The analysis of the electronic densities and potentials was carried out using GPAW[23,24] and the local density approximation (LDA).[25] The electron densities of the limiting bilayer configurations were computed using a grid expansion with 0.15 Å spacing and a $18 \times 18 \times 1$ $\boldsymbol{k}$-point mesh. Here, a compensating dipole layer was included in the Poisson solver.

III. RESULTS

The TMDs with MX_2 (M=Mo,W;X=S,Se) constitute a class of materials with similar behavior and here we therefore only carry out computations for large explicit moiré superlattices for the MoS_2/MoS_2 homobilayer. Computations and analysis of the limiting bilayer stackings have, however, been performed for all homobilayers and lattice constant matched heterobilayers.

A. Structural properties

First we report the computations of the interlayer distance, which is of fundamental importance since the wave function overlap of the constituent monolayer states is sensitively dependent on the interlayer distance. Therefore, both polarization and hybridization magnitude depend on the interlayer distance. In the zero-angle limit configurations, the interlayer distance for MoS_2/MoS_2

varies between 6.86 Å in R_h^h and 6.10 Å in R_h^X and R_h^M in decent agreement with other theoretical estimations.[26]

In moiré superlattices the interlayer distance varies with the lateral position. In order to quantify the interlayer distance for the explicit moiré structures, we therefore consider the distribution of distances (Fig. 3a), which we obtain by centering a cylinder of radius 3 Å on a transition metal atom in the upper layer and then taking the interlayer distance as the vertical distance between transition metal atoms found within the same cylinder.

At the largest considered twist angle (13°) the interlayer distance is rather homogeneous with a value roughly equal to the mean of the interlayer distance in R_h^h and R_h^X. This is not surprising since the interlayer interaction is very weak due to its van-der-Waals nature while the deformation of the monolayer sheets requires bending the much stronger covalent bonds. As the twist angle decreases the distribution widens. The extrema occur at R_h^h and R_h^M (R_h^X) and the local environment of the moiré superlattice at these specific points mimics the limiting configurations more and more as the twist angle decreases. The lower limit of the distribution shifts to smaller values (Fig. 3a) but even at the lowest twist angle considered, the smallest values are still slightly larger than the interlayer distance for the limiting R_h^X and R_h^M structures where the interlayer distance attains its minimum (which corresponds to the lower limit of the x-range in Fig. 3a).

One can also consider the distribution of the lateral displacements of the Mo atoms relative to the ideal moiré superlattice ($\delta d_{xy}^{\mathrm{Mo}}$) that appear during relaxation (Fig. 3b-e). The largest twist angle shown is 7.34° in which the maximal lateral displacement of the Mo atoms is 0.025 Å. For the smallest twist angle (4.41°), the maximum relaxation distance of the Mo atoms is significantly larger at 0.065 Å. For the 4.41° twist angle, the planar displacements forms three bands (Fig. 3e) corresponding to different distances of the displaced atom from the rotation center with a local AA stacking order. The direction of the lateral displacements for the Mo atoms is shown in Fig. 1b. The regions around the high symmetry points are almost vertically aligned and exhibit very little relaxation. The main relaxation occurs between high symmetry point R_h^h and R_h^X (and between R_h^M and R_h^h).

B. Moiré potential

Next we turn to the moiré potential. In Fig. 4a, a schematic illustration of the vacuum level difference (Eq. 3) as a function of displacement along the long diagonal of the unit cell is shown. The minimum occurs at R_h^X while the maximum occurs at R_h^M. The origin of the spatially varying vacuum level difference is the stacking dependent density polarization (Fig. 4b-d), which gives rise to asymmetric (with respect to the plane halfway between the monolayers) potentials (Fig. 4e-g). The potentials shown in (Fig. 4e-g) would correspond to the *interlayer* moiré potential at these specific sites within the moiré superlattice and the magnitude of this potential is around 80 meV for the MoS_2/MoS_2 homobilayer. Due to symmetry, this is also the full variation of the *intralayer* moiré potential, and taken together it places the full variation of the *interlayer* moiré potential at around 160 meV for this system.

We have also studied the twist angle dependence of the *intralayer* moiré potential by considering the maximal planar variation of the core potentials (Fig. 5). We find that it decays rapidly with increasing twist angle and already at $\sim 5°$ it has decayed to half of the zero limit value. Part of this decay can likely be explained by the increasing minimal interlayer distance with increasing twist angle and partly by the deviation from ideal stacking at R_h^X and R_h^M. This behavior of the moiré potential is consistent with explicit calculations of the $MoS_2/MoTe_2$ system,[7] with measured energy barriers of exciton diffusion in twisted $MoSe_2/WSe_2$[27] and in the localization of excitons in MoS_2/WS_2.[28]

The twist angle dependence of the moiré potential was computed without dipole corrections. In order to validate this approach we performed a test with an out-of-plane lattice vector of 100 Å and compared it with the 70 Å results. We found that the maximal planar variation of the Mo core potential for the 6.01° structure was 26.1 meV in both cases confirming that the spurious electric field does not influence the results.

C. Hybridization and tunneling in MoS_2/MoS_2

The electrostatic moiré potential rigidly shifts the single particle electronic states according to Eq. (4). The bilayer states are, however, subject to interlayer hybridization as well, which for MoS_2/MoS_2 homobilayer is quantified in Fig. 6 along the path between the Γ and K points. In all configurations, the hybridization contribution to the valence band shifts is small at the K point and large at Γ. For the conduction band, the hybridization contribution is largest at Λ (halfway between Γ and K). At the Γ point the hybridization is much stronger in R_h^X and R_h^M than for R_h^h. At K, on the other hand, the valence band hybridization is slightly larger in R_h^h (15 meV) compared to R_h^X, and R_h^M (5 meV) despite exhibiting a much larger interlayer distance. For the conduction band at K in R_h^X, and R_h^M the hybridization contribution is negative with a value of −2 meV.

The tunneling rates defined in Eq. (6) largely follow the hybridization energy but become imaginary when the hybridization energy is negative, which implies that the solution becomes non-physical (Sect. IV). This occurs at the Λ point for the valence band and the K point for the conduction band in R_h^X, and R_h^M. The tunneling rate at Λ for the conduction band is 132 meV in R_h^h rising to 184 meV in R_h^X and R_h^M. The tunneling rate for the K point is 2 meV (conduction band) and 15 meV (valence band) in R_h^h. The latter value rises to 19 meV in R_h^X and

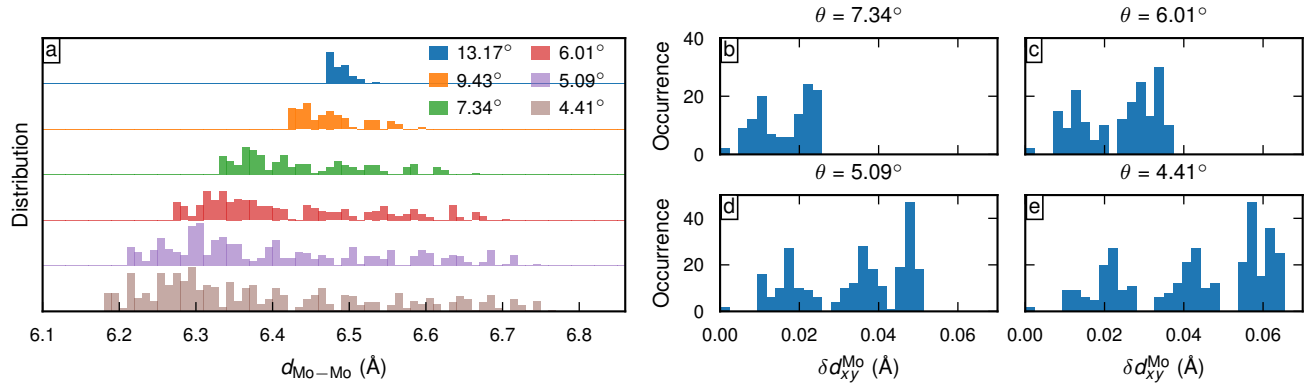

FIG. 3. (a) Distribution of interlayer distances in MoS_2/MoS_2 homobilayer as a function of twist angle. The lower and upper limits of the x-axis correspond to the layer spacing in R_h^h and R_h^M/R_h^X, respectively. (b–e) The distribution of lateral relaxation for the four lowest twist angles.

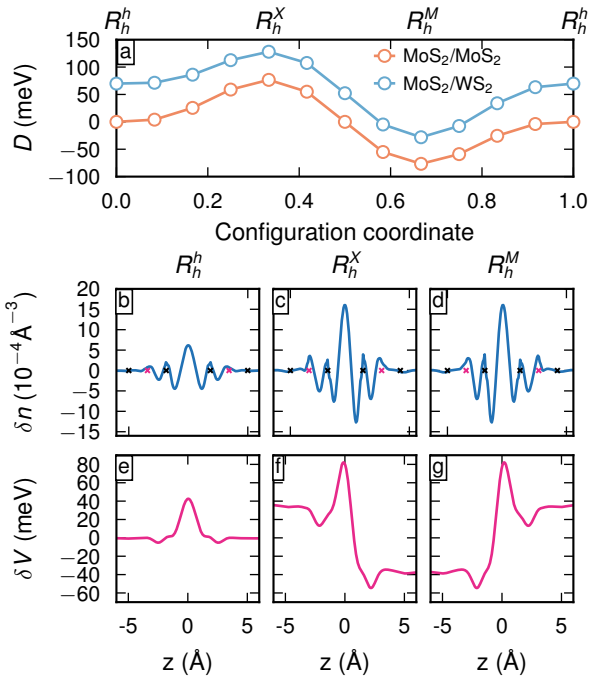

a

FIG. 4. (a) Schematic illustration of the vacuum level difference (Eq. 3) obtained by displacing the upper layer along the long diagonal of the primitive cell, keeping the interlayer distance fixed. (b-d) electron density (δn of Eq. 2) averaged in-plane for configurations R_h^h, R_h^X, and R_h^M of MoS_2/MoS_2. (e-g) Corresponding potential δV averaged in-plane.

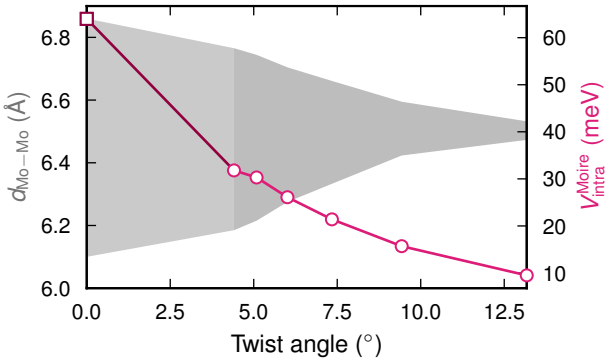

FIG. 5. Maximal planar variation of the core potential for MoS_2/MoS_2 moiré superlattices. 4.41° is the smallest twist angle for which explicit computations have been performed. The data point (indicated by a square) at 0° is the zero degree limit computed as the Mo core potential difference at R_h^h and the connecting line is a guide to the eye. The gray area indicates the range between the smallest and largest interlayer distance.

R_h^M while the former becomes imaginary. It was shown in Ref. 29 that the tunneling rate at K vanished in R_h^X and R_h^M under the assumption that the orbital character of the monolayer band edges were completely composed of transition metal d states. We attribute the appearance of a finite tunneling rate for the valence band at R_h^X and R_h^M at K to orbital mixing with other states. Based on semi-local DFT calculations, it was found in Ref. 30 that there is a minor but non-zero contribution to the band edge states coming from the chalcogen species.

The tunneling rates at Λ and K for R_h^h and R_h^X are to a good approximation linear in the interlayer distance (Fig. 7). In R_h^h, the interlayer dependence is stronger for both the states at Λ compared with K, whereas the dependence is very weak for the conduction band states. In R_h^X, the conduction band at Λ and the valence band at K exhibit stronger interlayer dependence than the other two states considered.

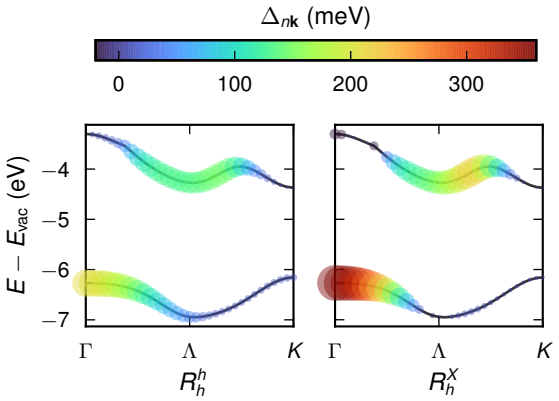

FIG. 6. Average hybridization contribution according to Eq. (5) of the valence band and conduction band for the limiting configurations of MoS_2/MoS_2 between the Γ and K points superimposed on the monolayer bands computed within the LDA.

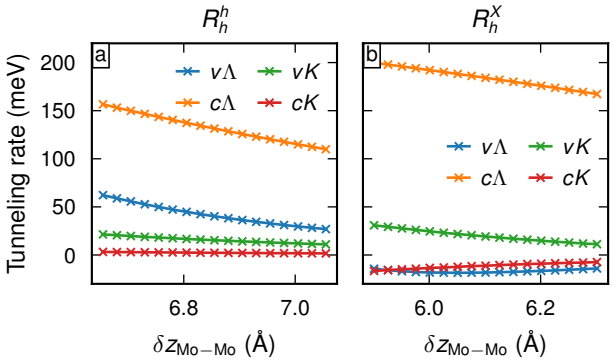

FIG. 7. Tunneling rates as a function of interlayer distance for (a) R_h^h and (b) R_h^X of MoS_2 homobilayer.

D. Extension to other TMDs

In Fig. 8 the vacuum level difference D as defined in Eq. (3) is shown for all Mo and W-based TMDs including the heterobilayers. For the homobilayers, the magnitude of the vacuum level difference is more or less uniform with minor variations between different TMDs despite rather large differences in the interlayer distance.

For the heterostructures, in contrast to the homobilayers, there is a vacuum level splitting present in R_h^h due to the presence of different transition metals. However, the full variation of the interlayer moiré potential is still rather similar over both the homobilayers and heterobilayers with an average of 131 meV (standard deviation is 8 meV). This is likely due to the fact that the relevant orbital character of all the TMDs considered are similar.

E. Excitons in TMD bilayers

We have briefly investigated how the layer dependent polarization and hybridization influence the exciton spectrum in the different stackings originating from the AA stacked system. The present analysis has been performed by solving the Wannier equation in a basis of the constituent monolayers (see Eq. (7)) and the resulting excitons contains both intra and inter-layer components[31,32] (Fig. 2).

The exciton spectra were investigated for the two prototype cases *i*) homobilayer WS_2, and *ii*) the $MoSe_2/WSe_2$ heterobilayer. In Fig. 9, the energy of the lowest lying exciton peak relative to the $K-K$ exciton in the R_h^h stacked structure is shown for the WS_2 homobilayer, and in Fig. 10, the same data is shown for the $MoSe_2/WSe_2$ heterobilayer. The transparent bars include the polarization shift but not the hybridization energy. For the homobilayer, the lowest $K-K$ exciton is of intralayer nature and hence the stacking dependent polarization does not affect the position of the peak. In particular, there is a very weak hybridization of the $K-K$ excitons. For the case of excitons that involve the $K-\Lambda$ valleys, the energy is around 150 meV lower than the R_h^h $K-K$ exciton with the largest contribution stemming from the hybridization of the conduction band at the Λ point. To properly see the effect of hybridization, we consider the $\Gamma-K$ exciton in the R_h^M stacking. Without accounting for hybridization, the exciton energy is about 200 meV higher in energy in comparison with the R_h^h $K-K$ exciton, since the valence band maximum (VBM) at Γ is lower in energy in comparison with at the K-point. The VBM at Γ is pushed to higher energies by hybridization and the exciton energy becomes lower than the R_h^h $K-K$ exciton. The $\Gamma-\Lambda$ indirect exciton is the one mostly affected by the hybridization since it is strong in both these valleys.

In the heterobilayer however, where the lowest exciton exhibits interlayer character, there is a pronounced effect of the polarization field on the lowest $K-K$ exciton and the exciton energy difference between the different stacking orders corresponds to the variation of the dipole field. The $K-\Lambda$ exciton is, without accounting for hybridization located around 150 meV-200 meV above the R_h^h exciton. This energy drops significantly due to hybridization pushing the Λ valley to lower energies. In contrast to the case of the homobilayer where the indirect $\Gamma-K$ exciton is lower in energy with respect to the R_h^h $K-K$ exciton, the $\Gamma-K$ exciton in the heterobilayer has a much larger energy in comparison with the R_h^h $K-K$ exciton.

IV. DISCUSSION

The main result of this study is that the moiré potential exhibits a strong twist angle dependence, as is evident from Fig. 5. The origin of this potential is an

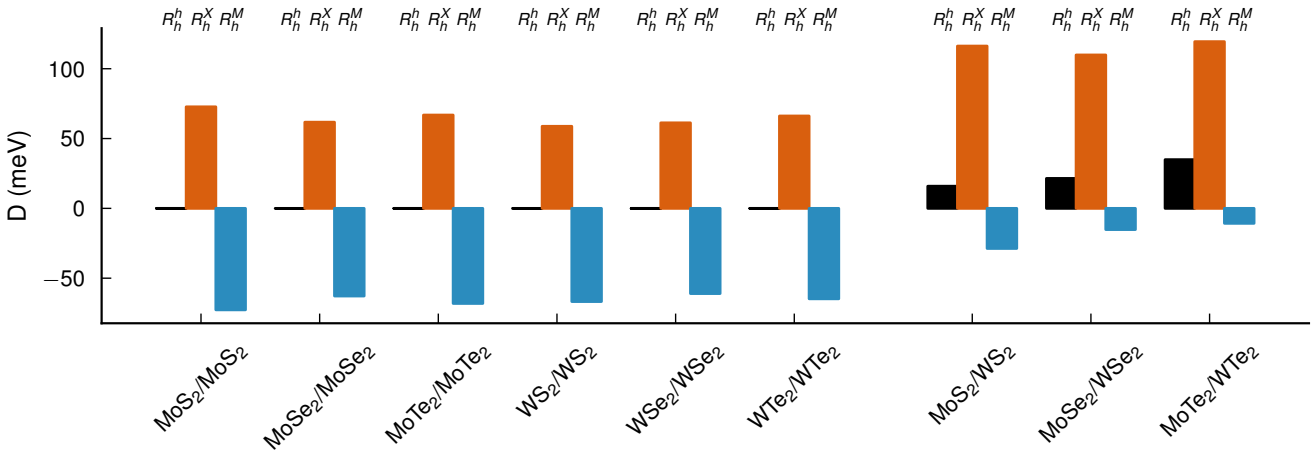

FIG. 8. Maximal variation of the dipole field for homobilayers and heterobilayers at the limiting configurations according to Eq. (3).

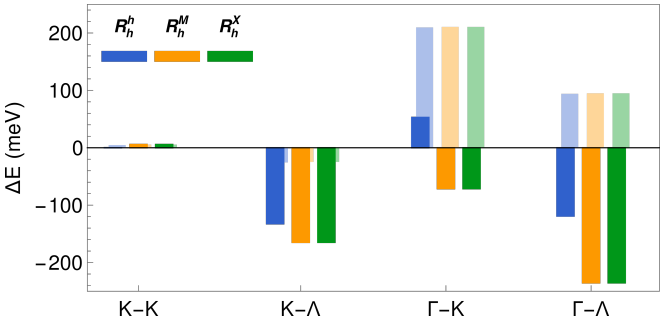

FIG. 9. Energy of the lowest exciton peak relative to the lowest $K(\text{hole}) - K(\text{electron})$ exciton for the WS_2 homobilayer. The shaded bars indicate the influence of the polarization shift and the solid bars indicate the influence of both the polarization shift and hybridization.

asymmetric charge density displacement that is dependent on the twist angle. The twist angle dependence of the potential can be traced back to the varying interlayer distance and the horizontal alignment. The latter was suggested to be the explanation for the twist angle dependence of the band gap in the twisted heterostructure $MoS_2/MoTe_2$[7] and is likely to be the dominating contribution to the twist angle dependence of the moiré potential in MoS_2/MoS_2 as well.

The implications of a twist angle dependent potential are manifold. For example, it determines for which angles the electronic states at the band edges become localized. Furthermore, the twist angle dependence has implications for the temporal localization of charge carriers, since the potential is effectively an energy barrier. One of the charge carriers will be subject to an energy barrier induced by the dipole potential. For example, the transition from the lowest hole potential configuration to R_h^h raises the hole energy by $D/2$. With increasing twist angle the energy barrier becomes smaller. Therefore, it is expected that the temporal localization of charge carriers is strongest at very small twist angles.

Exciton migration may proceed via resonant energy transfer[28] but in the case that electron and hole migrate separately the current results are consistent with measurements on exciton diffusion. The interlayer exciton diffusion in $MoSe_2/WSe_2$ was investigated in Ref. 33 and it was found that the exciton diffusion was considerably larger at a 3.5° twist angle than a 1° twist angle.

The numerical values of the dipole field amplitude D are quite similar for all the TMDs considered here (Fig. 8). The similarity of D despite vastly different interlayer distances is interesting in itself and suggests that the dipole field is primarily a geometrical property, which, together with orbital similarity across this class of materials, results in a similar magnitude. In fact, the interlayer distance and the induced density difference (δn) are not independent quantities. The density difference forms mainly between the layers, creating a bonding electron density that is slightly polarized, which in turn gives rise to an electric field that balances the bonding electron density and dispersion interaction.

The moiré potential affects inter and intralayer excitons differently in the bilayer structures (Fig. 9 and Fig. 10) and the energy for the $K - K$ exciton with interlayer character exhibits an energy variation over the stacking orders R_h^h, R_h^X, and R_h^M that closely resembles the dipole field magnitude. The tunneling rates at the conduction band at K and the valence band at Λ are imaginary at R_h^X and R_h^M with similar values of around $10i - 20i$ meV. While the Λ valence band is largely irrelevant due to its low energy, the conduction band at K is rather important for the excitonic spectra. The tunneling rates are, as constructed, off-diagonal components to a perturbation of the two-level system consisting of the equivalent band from different monolayers. In this case,

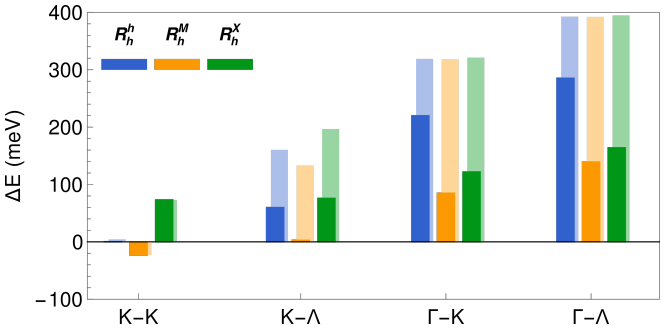

FIG. 10. Energy of the lowest exciton peak relative to the lowest K(hole) − K(electron) exciton for the $MoSe_2/WSe_2$ heterobilayer. The shaded bars indicate the influence of the polarization shift and the solid bars indicate the the influence of both the polarization shift and hybridization.

the splitting of the levels in the bilayer system is smaller than the difference in potential shift between the states. The tunneling matrix element represents the interaction that causes band edge shifts that go beyond the splitting that is caused by potential alignment. To describe this effect, here we employ a simple two-band model, see Eq. (6). The appearance of imaginary solutions can be attributed the breakdown of this approximation and signify that the bilayer energy shifts are influenced by coupling to multiple states.

V. CONCLUSIONS

To summarize, we have shown that the moiré potential in TMDs exhibits both an electrostatic component and a hybridization component, which are intertwined and have different relative strengths in different parts of the Brillouin zone. The electrostatic component of the moiré potential is a varying dipole field, which has a strong twist angle dependence. In some cases, the hybridization component can be interpreted as a tunneling rate but the interpretation is not generally applicable over the full Brillouin zone.

ACKNOWLEDGMENTS

Funding from the Knut and Alice Wallenberg Foundation (2014.0226, 2019.0140) as well as the Swedish Research Council (2020-04935, 2018-06482) are gratefully acknowledged. The Marburg group acknowledges support from Deutsche Forschungsgemeinschaft (DFG) via SFB 1083 (Project B9) and the European Unions Horizon 2020 research and innovation program under grant agreement No 881603 (Graphene Flagship). The computations were enabled by resources provided by the Swedish National Infrastructure for Computing (SNIC) at C3SE and HPC2N partially funded by the Swedish Research Council through grant agreement no. 2018-05973.

* erhart@chalmers.se

[1] M. H. Naik and M. Jain, Physical Review Letters **121**, 266401 (2018).
[2] S. Brem, C. Linderälv, P. Erhart, and E. Malic, Nano Letters **20**, 8534 (2020).
[3] H. Yu, G.-B. Liu, J. Tang, X. Xu, and W. Yao, Science Advances **3** (2017), 10.1126/sciadv.1701696.
[4] D. A. Ruiz-Tijerina and V. I. Fal'ko, Physical Review B **99**, 125424 (2019).
[5] X. Lu, X. Li, and L. Yang, Physical Review B **100**, 155416 (2019).
[6] S. Shabani, D. Halbertal, W. Wu, M. Chen, S. Liu, J. Hone, W. Yao, D. N. Basov, X. Zhu, and A. N. Pasupathy, Nature Physics (2021), 10.1038/s41567-021-01174-7.
[7] W. T. Geng, V. Wang, J. B. Lin, T. Ohno, and J. Nara, The Journal of Physical Chemistry C **125**, 1048 (2021).
[8] J. M. B. Lopes dos Santos, N. M. R. Peres, and A. H. Castro Neto, Physical Review Letters **99**, 256802 (2007).
[9] A. Kormányos, G. Burkard, M. Gmitra, J. Fabian, V. Zólyomi, N. D. Drummond, and V. Fal'ko, 2D Materials **2**, 022001 (2015).
[10] Q. Tong, M. Chen, F. Xiao, H. Yu, and W. Yao, 2D Materials **8**, 025007 (2020).
[11] J. Hagel, S. Brem, C. Linderälv, P. Erhart, and E. Malic, Physical Review Research **3**, 043217 (2021).
[12] A. L. Ivanov and H. Haug, Physical Review B **48**, 1490 (1993).
[13] M. Selig, G. Berghäuser, M. Richter, R. Bratschitsch, A. Knorr, and E. Malic, 2D Materials **5**, 035017 (2018).
[14] F. Katsch, M. Selig, A. Carmele, and A. Knorr, physica status solidi (b) **255**, 1800185 (2018).
[15] S. Brem, K.-Q. Lin, R. Gillen, J. M. Bauer, J. Maultzsch, J. M. Lupton, and E. Malic, Nanoscale **12**, 11088 (2020).
[16] Y. Wang, Z. Wang, W. Yao, G.-B. Liu, and H. Yu, Physical Review B **95**, 115429 (2017).
[17] P. E. Blöchl, Physical Review B **50**, 17953 (1994).
[18] A. H. Larsen, J. J. Mortensen, J. Blomqvist, I. E. Castelli, R. Christensen, M. Dułak, J. Friis, M. N. Groves, B. Hammer, C. Hargus, E. D. Hermes, P. C. Jennings, P. B. Jensen, J. Kermode, J. R. Kitchin, E. L. Kolsbjerg, J. Kubal, K. Kaasbjerg, S. Lysgaard, J. B. Maronsson, T. Maxson, T. Olsen, L. Pastewka, A. Peterson, C. Rostgaard, J. Schiøtz, O. Schütt, M. Strange, K. S. Thyge-

sen, T. Vegge, L. Vilhelmsen, M. Walter, Z. Zeng, and K. W. Jacobsen, Journal of Physics: Condensed Matter **29**, 273002 (2017).
[19] G. Kresse and J. Hafner, Physical Review B **47**, 558 (1993).
[20] G. Kresse and J. Furthmüller, Computational Materials Science **6**, 15 (1996).
[21] M. Dion, H. Rydberg, E. Schröder, D. C. Langreth, and B. I. Lundqvist, Physical Review Letters **92**, 246401 (2004).
[22] K. Berland and P. Hyldgaard, Physical Review B **89**, 035412 (2014).
[23] J. J. Mortensen, L. B. Hansen, and K. W. Jacobsen, Physical Review B **71**, 035109 (2005).
[24] J. Enkovaara, C. Rostgaard, J. J. Mortensen, J. Chen, M. Dułak, L. Ferrighi, J. Gavnholt, C. Glinsvad, V. Haikola, H. A. Hansen, H. H. Kristoffersen, M. Kuisma, A. H. Larsen, L. Lehtovaara, M. Ljungberg, O. Lopez-Acevedo, P. G. Moses, J. Ojanen, T. Olsen, V. Petzold, N. A. Romero, J. Stausholm-Møller, M. Strange, G. A. Tritsaris, M. Vanin, M. Walter, B. Hammer, H. Häkkinen, G. K. H. Madsen, R. M. Nieminen, J. K. Nørskov, M. Puska, T. T. Rantala, J. Schiøtz, K. S. Thygesen, and K. W. Jacobsen, Journal of Physics: Condensed Matter **22**, 253202 (2010).
[25] J. P. Perdew and A. Zunger, Physical Review B **23**, 5048 (1981).
[26] K. Liu, L. Zhang, T. Cao, C. Jin, D. Qiu, Q. Zhou, A. Zettl, P. Yang, S. G. Louie, and F. Wang, Nature Communications **5**, 4966 (2014).
[27] Z. Li, X. Lu, D. F. Cordovilla Leon, Z. Lyu, H. Xie, J. Hou, Y. Lu, X. Guo, A. Kaczmarek, T. Taniguchi, K. Watanabe, L. Zhao, L. Yang, and P. B. Deotare, ACS Nano **15**, 1539 (2021).
[28] H. Guo, X. Zhang, and G. Lu, Science Advances **6** (2020), 10.1126/sciadv.abc5638.
[29] Q. Tong, H. Yu, Q. Zhu, Y. Wang, X. Xu, and W. Yao, Nature Physics **13**, 356 (2017).
[30] S. Haastrup, M. Strange, M. Pandey, T. Deilmann, P. S. Schmidt, N. F. Hinsche, M. N. Gjerding, D. Torelli, P. M. Larsen, A. C. Riis-Jensen, J. Gath, K. W. Jacobsen, J. J. Mortensen, T. Olsen, and K. S. Thygesen, 2D Materials **5**, 042002 (2018).
[31] S. Ovesen, S. Brem, C. Linderälv, M. Kuisma, T. Korn, P. Erhart, M. Selig, and E. Malic, Communications Physics **2**, 23 (2019).
[32] P. Merkl, F. Mooshammer, P. Steinleitner, A. Girnghuber, K.-Q. Lin, P. Nagler, J. Holler, C. Schüller, J. M. Lupton, T. Korn, S. Ovesen, S. Brem, E. Malic, and R. Huber, Nature Materials **18**, 691 (2019).
[33] J. Choi, W.-T. Hsu, L.-S. Lu, L. Sun, H.-Y. Cheng, M.-H. Lee, J. Quan, K. Tran, C.-Y. Wang, M. Staab, K. Jones, T. Taniguchi, K. Watanabe, M.-W. Chu, S. Gwo, S. Kim, C.-K. Shih, X. Li, and W.-H. Chang, Science Advances **6**, eaba8866 (2020).